

Self-Consistent Hopping Theory of Activated Relaxation and Diffusion of Dilute Penetrants in Dense Crosslinked Polymer Networks

Baicheng Mei ^{a,d}, Tsai-Wei Lin ^{c,d}, Charles E. Sing ^{a,c,d} and Kenneth S. Schweizer ^{*a,b,c,d}

^a Department of Materials Science, University of Illinois, Urbana, IL 61801

^b Department of Chemistry, University of Illinois, Urbana, IL 61801

^c Department of Chemical & Biomolecular Engineering, University of Illinois, Urbana, IL 61801

^d Materials Research Laboratory, University of Illinois, Urbana, IL 61801

^{} kschweiz@illinois.edu*

Abstract

We generalize and apply a microscopic force-level statistical mechanical theory of the activated dynamics of dilute spherical penetrants in glass-forming liquids to study the influence of permanent crosslinking in polymer networks on the relaxation time and diffusivity over a wide range of temperature and crosslink density. The theory treats network crosslinkers as locally pinned or vibrating sites. Calculations are performed for model parameters relevant to recent experimental studies of a nm-sized organic dye diffusing in crosslinked poly(n-butyl methacrylate) networks. The theory predicts the penetrant alpha time increases exponentially with the crosslink fraction (f_n) dependent glass transition temperature, T_g , which grows roughly linearly with the square root of crosslink density. Moreover, we find that T_g is also proportional to an entropic geometric confinement parameter defined as the ratio of the penetrant diameter to the mean mesh size. The decoupling of the ratio of the penetrant and Kuhn segment alpha relaxation times displays a complex non-monotonic dependence on crosslink density and temperature via the variable $T_g(f_n)/T$, but a remarkably good collapse is predicted. The microscopic mechanism for activated penetrant relaxation is elucidated based on the theoretically predicted crosslink fraction dependent coupled local cage and nonlocal collective elastic barriers. A model for the penetrant diffusion constant that combines glassy physics and entropic mesh confinement is proposed which results in a significantly stronger suppression of mass transport with degree of effective supercooling than predicted for the penetrant alpha relaxation time. This represents a unique polymer network-based type of “decoupling” of diffusion and relaxation. In contrast to the diffusion of larger nanoparticles in high temperature rubbery polymer networks, our analysis suggests that for the penetrants studied the mesh confinement effects are of secondary importance in the highly supercooled regimes of interest relative to the consequences on mass transport of crosslink-induced slowing down of activated segmental relaxation. Support for the theoretical predictions from our complementary simulation study is briefly discussed.

I. Introduction

Understanding and controlling molecular (“penetrant”) transport in dense and cold polymer melts, crosslinked networks, and glasses is a problem of high basic polymer physics interest^[1-14] that also underpins advanced separation membrane applications^[10-27]. However, even in the *dilute* penetrant limit of interest in this work, existing theoretical models are highly phenomenological, often built on the difficult to uniquely define and unambiguously predict concept of “free volume”.^[13, 27-33]

Recently, two of us have pursued the construction of a statistical mechanical theory (the Self Consistent Cooperative Hopping (SCCH) theory) for penetrant activated dynamics in polymer melts ^[34]. The foundation is the Elastically Collective Nonlinear Langevin Equation (ECNLE) theory^[35, 36] for the thermally activated structural (alpha) relaxation process on the Kuhn segment scale in one-component melts^[37]. This approach is microscopic in the sense that it causally relates pair interactions, thermodynamic state, and packing structure as embedded in a dynamic free energy which quantifies kinetic constraints. The alpha relaxation is a coupled local-nonlocal activated process characterized by a local cage barrier ($F_{B,K}$) associated with large-amplitude activated hopping coupled with collective long-range (nonlocal) small displacements of all segments outside the cage characterized by an elastic barrier ($F_{el,K}$). Recent studies support the predictions of this approach for a large number of real-world polymeric liquids, including olefins, dienes, siloxanes, and vinyl polymer chemistries.^[38-40] Chemical crosslinking introduces new kinetic constraints and additional dynamical slowing down. ECNLE theory has been very recently extended to polymer networks and shown to provide an excellent understanding of experiments on poly(n-butylacrylate) (PnBA) networks and coarse-grained simulations over a wide range of crosslink densities and temperatures.^[41]

SCCH theory for dilute hard sphere penetrants (diameter, d) in a hard-sphere matrix [42, 43] or semi-flexible polymer melts [34] under structurally equilibrated conditions has been extensively applied, and many of its predictions agree well with simulations [7, 42] and experiments [44]. The penetrant activation barrier and mean hopping time, and the extent of coupling of penetrant transport with the early, medium, and late stages of the matrix structural relaxation process, are self-consistently predicted based on two *coupled* dynamic free energies.[34, 42, 43, 45]

The goal of the present work is to formulate and apply SCCH theory to permanent crosslinked polymer networks. We are especially motivated by recent measurements of Evans and coworkers on the diffusion of a dilute aromatic molecule [N,N'-Bis(2,5-di-tert-butylphenyl)-3,4,9,10-perylenedicarboximide (BTBP)] in crosslinked PnBA networks over a wide range of crosslink densities at fixed temperature.[9] The experiments found that the penetrant alpha time and diffusion constant both vary exponentially with the crosslink fraction (f_n) dependent network glass transition temperature $T_g(f_n)$, but their quantitative dependences on $T_g(f_n)$ and T are different, a form of “decoupling” in the language of glass physics. The precise physical mechanisms at play remain unclear. For example, is the apparent decoupling a consequence of entropic mesh confinement constraints on penetrant motion in crosslinked networks? Alternatively, is the glass physics mechanism associated with the dynamic heterogeneity (DH)[46-48] driven breakdown of the Stokes-Einstein breakdown relation [49-54] in supercooled liquids relevant? Or is there another explanation?

The mesh confinement effect has been studied theoretically[55], experimentally[9], and with simulation[56,57] for the problem of the motion of a dilute spherical nanoparticle (larger than typical molecules) in polymer networks. A key variable is the confinement parameter, $C = d/a_x$, where a_x is the mean mesh size that decreases with crosslink density. For example, the polymer physics

model of Cai-Panykov-Rubinstein (CPR) [55] predicts that when mesh confinement is strong enough ($C > 1$) the nanoparticle diffusion constant is:

$$D_p \propto \frac{d^2}{\tau_R} \exp(-C^2)/C \equiv \frac{d^2}{\tau_R} X \quad (1)$$

where $\tau_R \sim N_x^2 \tau_\alpha$ is the Rouse time of a network strand composed of N_x segments, the segmental alpha time, τ_α , depends on temperature but is assumed to *not* vary with crosslink density, and the quantity $X(C)$ is defined which quantifies the explicit entropic effect of a physical mesh. Such a model is most germane to the high temperature rubbery regime. Recently, a simulation study of such a semi-dilute solution model in the high temperature rubbery regime has been performed [57], and finds $\log(1/CD_p) \propto C^2$ for *both* $C > 1$ and $C < 1$. By revisiting their data, we find the prefactor between $\log(1/CD_p)$ and C^2 is significantly larger than $\log(e)$ in the CPR entropic mesh model, suggesting the kinetic factor $\frac{d^2}{\tau_R}$ in Eq.(1) must also contribute significantly to the crosslink density dependence of the penetrant diffusion constant and may also vary exponentially with $-C^2$ for unknown reasons. Qualitatively, this is what we expect within the SCCH theory of penetrant diffusivity given our recent ECNLE theory of segmental relaxation in polymer networks (and the complementary experiment and simulations) found the alpha time of polymer Kuhn segments increases strongly with crosslink fraction[41] which must have a significant impact on the penetrant alpha relaxation process.

Given the above, in this article we propose and test the idea that the penetrant diffusion constant in Eq.(1) should scale inversely with the activated “penetrant alpha time” yielding:

$$D_p \propto \frac{d^2}{\tau_{\alpha,p}} \exp(-C^2)/C \equiv \frac{d^2}{\tau_{\alpha,p}} X \propto \exp(-BC^2)/C \quad (2)$$

where $\tau_{\alpha,p}$ is both temperature and crosslink density dependent, and B is a chemistry specific numerical factor. We note that since in most real world situations the molecular penetrants do not

obey the strong mesh confinement inequality $C > 1$, other workers [56] have considered, and explored with simulation, an alternative model of the effect of the mesh confinement corresponding to a penetrant entropic barrier scaling linearly with the confinement parameter, $D_p \propto \frac{d^2}{\tau_R} \exp(-b'C)$. If one adopts this description of mesh confinement effects, then our proposal in Eq.(2) becomes:

$$D_p \propto \frac{d^2}{\tau_{\alpha,p}} \exp(-b'C) \propto \exp(-EC) \quad (3)$$

Here, and in our companion simulation paper [58], we adopt SCCH theory to quantitatively analyze the effect of crosslinking effect on the penetrant alpha relaxation time and diffusion constant in the specific context of the well-studied PnBA networks. In general, the penetrant alpha relaxation time and diffusion constant are high-dimensional functions, depending on variables such as temperature, penetrant chemistry (size and shape), penetrant-polymer interaction, polymer persistence or Kuhn length, and degree of crosslinking (or mesh size). To render the analysis tractable, we consider a single spherical penetrant of diameter that mimics BTBP [9,59] (having the same volume, 735.88 \AA^3 , corresponding to $d=1.12\text{nm}$) and a purely repulsive penetrant-polymer interaction (reasonable for the nonpolar dye molecule) and a polymer model calibrated for PnBA networks, and focus on how temperature, crosslink density, and mesh size impact $\tau_{\alpha,p}$ and D_p . This choice of penetrant size and the range of crosslink fractions studied allows us to probe confinement parameters from well below unity to modestly above unity, as germane to the typical molecular penetrant problem. When $C \gg 1$, penetrant motion in the melt will be slaved to the polymer segmental relaxation time, and in permanent networks will be effectively quenched.

Section II briefly describes ECNLE theory and its extension to crosslinked polymer networks, and presents some new calculations relevant to the penetrant work in this article. SCCH theory is briefly reviewed in section III, and the calculation of foundational theoretical quantities

required to predict penetrant alpha relaxation time and diffusion constant are presented. The penetrant relaxation time and its relationship to the network glass transition temperature and mesh confinement parameter are systematically studied in section IV. The question of the degree of decoupling between the penetrant and polymer segmental relaxation times is analyzed in section V. The role of crosslinking on the penetrant diffusion constant is studied in section VI, and the effects of crosslink-induced mesh confinement versus prolongation of network segmental relaxation on penetrant transports are disentangled. The article concludes in section VII with a summary and future outlook. Throughout the paper we comment on the comparison of our theoretical results with our companion simulation study at the level of qualitative and semi-quantitative trends.

Finally, we emphasize that nearly *all* the theoretical technical details, equations, derivations, numerical implementations, and discussion of limitations of the dynamic theories (ECNLE^[35-37, 41] and SCCH^[34, 42, 43, 45]) at the Kuhn scale and the Polymer Reference Interaction Site Model (PRISM) integral equation theory^[34, 37, 41] for the required structural pair correlation functions have been thoroughly documented in the literature and are not repeated here. The present paper is the first to include crosslinks in SCCH theory, but its analog for polymer melts has been discussed in detail ^[34]. Thus, our review of ECNLE theory in section II and SCCH theory in section III focuses on their physical content and key parameters, with mathematical development presented only for the new aspects of SCCH theory required to treat crosslinked networks.

II. ECNLE Theory of Structural Relaxation in Crosslinked Polymer Networks

A. Theoretical Background for Homopolymer Melts and Crosslinked Networks

The foundational starting point for predicting the activated dynamics of one-component spherical particle fluids is the single particle scalar displacement (r) - dependent dynamic free

energy, $F_{\text{dyn}}(r)$. The negative gradient of this quantity determines an effective force in a stochastic nonlinear Langevin equation that controls the spatially local aspect of activated barrier hopping trajectories and a local cage barrier (right panel of Fig.1).^[60] At sufficiently high (low) packing fraction (temperature), a particle jump distance is predicted to be sufficiently large (Δr_k) (see Fig.1) that in order for it to occur all the particles outside the cage must elastically displace in a dilational (cage expansion) collective manner by a small amount. This cage expansion sets the amplitude of the collective elastic displacement field.^[35, 36] and costs elastic energy. The resultant physical picture is that the alpha relaxation is a coupled local-nonlocal in space process (see middle panel of Fig.1), characterized by local cage and longer-range collective elastic barriers.

Recently, we extended ECNLE theory to homopolymer melts including the consequences of local chain connectivity and backbone stiffness on packing structure and dynamics ^[37, 41, 61]. Motivated by the theoretical arguments of Zhou and two of us ^[37], the Kuhn segment is adopted as the relevant dynamical length scale for the alpha process, and thus the scalar displacement of the rigid Kuhn segment (consisting of several bonded elementary sites) center-of-mass from its initial position, $r_K(t)$, is the central dynamical variable. The Kuhn segment is characterized by an effective *dynamically* correlated number of beads, N_K (see left panel of Fig.1) in a semiflexible Koyama model^[62, 63]. For typical polymers, $N_K \sim 2-3$, and in the present work we set $N_K = 2l_p$ with l_p the persistence length. The sensibility of this model construction has been quantitatively tested in prior combined simulation-theory work ^[37].

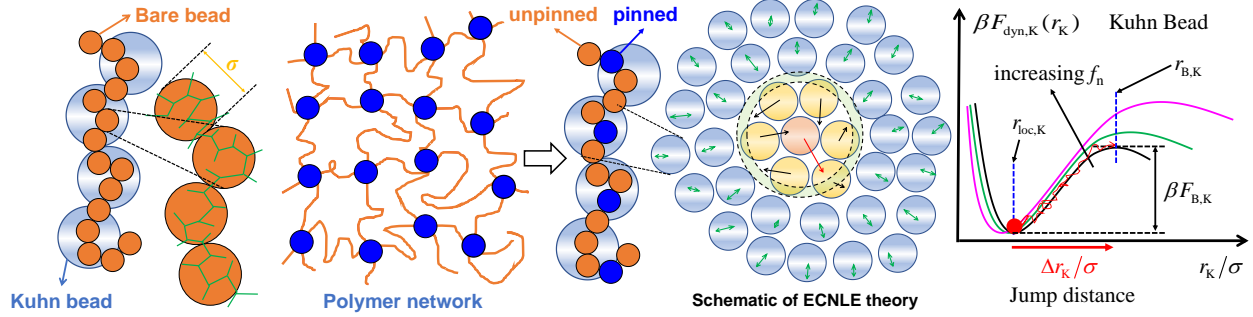


Fig.1. Left panel: Schematic of coarse-graining a polymer melt to the Kuhn scale and introduction of crosslinks based on pinning interaction sites in a regular manner along the chain. Middle panel: Schematic of the physical ideas of local-nonlocal relaxation mechanism within ECNLE theory shown for simplicity for a spherical particle liquid: activated particle hopping involves a local cage barrier and a longer-range cooperative elastic displacement of all particles outside the cage which induces an additional nonlocal elastic barrier. Right panel: Schematic of key features of the dynamic free energy as a function of dimensionless displacement of a Kuhn segment and its evolution with increasing crosslink fraction, f_n . The localization length $r_{loc,K}$ decreases with f_n , while the local cage barrier, barrier location $r_{B,K}$, and jump distance $\Delta r_K = r_{B,K} - r_{loc,K}$ all increase.

The local cage barrier $F_{B,K}$ is obtained directly from the dynamic free energy which is constructed solely from knowledge of the inter- and intra- molecular equilibrium pair correlation functions. The elastic barrier has been derived to be: $\beta F_{el,K} \approx 2\pi r_{cage,K}^3 \Delta r_{eff,K}^2 \rho_K K_{0,K}$, where $K_{0,K}$ is the harmonic curvature or spring constant at the localization length and the angularly averaged effective cage dilation amplitude is $\Delta r_{eff,K} \approx 3\Delta r_K^2 / 32r_{cage,K}$; both these quantities are computed from the dynamic free energy. The Kuhn scale ‘‘cage radius’’ is $r_{cage,K} = N_K^{1/3} r_{cage,m}$ with $r_{cage,m}$ being the location of the first minimum of polymer matrix radial distribution function $g_{mm}(r)$ at the elementary interaction site level and $\rho_K = \rho / N_K$ the number density of Kuhn segments.

Chemical crosslinking is modeled as follows [41]. First, it is assumed to not change the site-site intramolecular and intermolecular structural pair correlations. This simplification is consistent with a recent simulation study [64] that found the dimensionless compressibility of crosslink networks remains essentially unchanged compared to the melt. Second, a ‘‘neutral confinement’’ model of partial random pinning of particles (as widely studied in the glassy dynamics area) is

adopted which in the polymer network context mimics chemical crosslinking as a fraction (f_n) of dynamically immobile segments (zero localization length) distributed in a regular manner along a chain, per the schematic in Fig.1. The ratio $n_{\text{crosslink}}/(n_{\text{crosslink}} + n_{\text{monomer}})$ defines the crosslink fraction f_n , where $n_{\text{crosslink}}$ and n_{monomer} are the site (bare bead) level number of crosslinkers and normal mobile beads, respectively. Determination of the corresponding dynamic partial structure factors which enter as collective Debye-Waller factors [41, 61, 65] in the construction of the dynamic free energy is identical to prior work [41]. Crosslinkers modeled as pinned sites modify *all* aspects of ECNLE theory via the dynamic free energy.

The mean barrier hopping time $\tau_{\text{hop,K}}$ is then computed based on the Kramers mean first passage time theory as [41, 42, 66, 67]

$$\tau_{\text{hop,K}} = \frac{2\tau_{\text{s,K}} e^{\beta F_{\text{el,K}}}}{\sigma_{\text{K}}^2} \int_{r_{\text{loc,K}}}^{r_{\text{loc,K}} + \Delta r_{\text{K}}} dr_{\text{K}} e^{\beta F_{\text{dyn,K}}(r_{\text{K}})} \int_{r_{\text{loc,K}}}^{r_{\text{K}}} dr'_{\text{K}} e^{-\beta F_{\text{dyn,K}}(r'_{\text{K}})} \quad (4)$$

where $\tau_{\text{s,K}} = \sigma_{\text{K}}^2/D_{\text{s,K}}$ is a characteristic very short-time scale unaffected by crosslinking for a Kuhn unit ($\sigma_{\text{K}} = N_{\text{K}}^{1/3}\sigma$) and the formula for $D_{\text{s,K}}$ is given elsewhere [35, 41, 42]. Using the PRISM theory of equilibrium structural pair correlation functions as input to the dynamic free energy and hence Eq.(4), the mean Kuhn segment alpha relaxation time is computed numerically as $\tau_{\alpha,\text{K}} = \tau_{\text{s,K}} + \tau_{\text{hop,K}}$. To confront our theoretical results with experimental or simulation results, we adopt the elementary timescale of a Newtonian liquid, $\tau_0 = 16\phi\sigma(\beta M/\pi)^{1/2}$ as the time unit, which is typically ~ 1 ps, per prior studies [35, 41].

B. Mapping to Thermal Polymer Melts and Networks

To determine the required equilibrium site-site pair correlation functions, PRISM integral equation theory with the Percus-Yevick (PY) closure is employed.[41, 61] The penetrant and polymer interactions sites are modeled as hard spheres. The intramolecular structure factor of an

ideal semiflexible chain $\omega_{\text{mm}}(q)$, penetrant-to-matrix size ratio d/σ , and polymer site reduced density or packing fraction enter as inputs to PRISM theory, and $\omega_{\text{mm}}(q)$ is determined using the semiflexible tangent discrete Koyama model^[41, 62, 67]. This single chain statistical model is characterized by the bond length l_b , bead diameter l_d , and persistence length l_p ; we adopt its “tangent” version corresponding to $l_b = l_d = \sigma$. In our recent work on pure polymer network relaxation, a generic flexible chain persistence length of $l_p = \frac{4}{3}\sigma$ was adopted^[41]. In the present work, for the PnBA network the Kuhn length and monomer effective diameter are evaluated from experimental information to be $l_K = 1.72\text{nm}$ and $l_b = 0.72\text{nm}$, respectively, corresponding to a local aspect ratio $l_K/l_b = 2.4$, or in terms of the persistence length $l_p/\sigma = 1.2$. Since in the tangent Koyama model one has $\frac{l_K}{\sigma} = \frac{2l_p}{\sigma} - 1$, the adopted mapping yields $\sigma = 1.23\text{nm}$, which is slightly larger than $\sigma = 1.03\text{nm}$ if $l_p = \frac{4}{3}\sigma$ is chosen. The core theoretical predictions for the $l_p/\sigma = 1.2$ and $4/3$ models are very similar (see Appendix). In the main text we adopt the $l_p/\sigma = 1.2$ model.

To address experimental systems under isobaric (1 atm) conditions where temperature is the control variable, we adopt the well developed and tested mapping approach that relates in a chemistry specific manner the polymer packing fraction to temperature.^[39-41] Specifically, the dimensionless compressibility, $S_0(T)$, from PRISM theory for the semiflexible Koyama chain model^[41, 62, 67] is equated to that obtained from experimental equation of state (EOS) data^[44, 68] for PnBA melts.^[39-41] The result of this mapping is shown in the inset of Fig.2. A nearly linear dependence is valid from the very high temperature regime ($> 400\text{K}$) through the modestly supercooled regime, down to the glass transition temperature. The main frame of Fig.2 shows S_0 can be accurately represented by the analytic formula $S_0^{-1} = N_s(B/T - A')^2$ derived from the van der Waals model^[69] EOS. As discussed previously^[38, 69, 70], reasonable variation of N_s does not

affect our analysis since the crucial aspect is the T -dependence of S_0 that is determined by the EOS parameters A' and B , and N_s enters only as a T -independent prefactor. The final step of our model construction is to set $N_s = 7.75$ to reproduce the experimental glass transition temperature of $T_g = -45$ °C of pure PnBA melts [9].

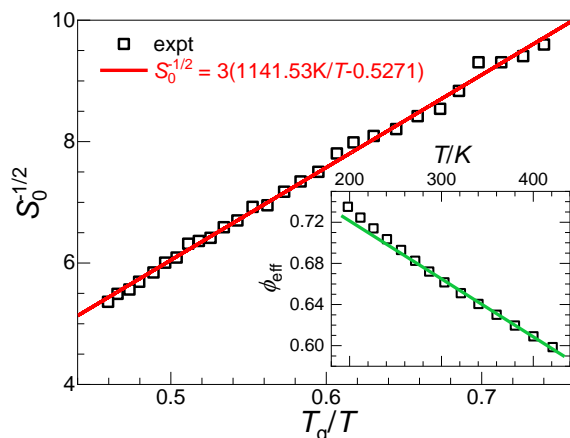


Fig. 2. Main: Experimental dimensionless compressibility data of PnBA melt versus scaled inverse temperature in a representation suggested by the van der Waals model [69]. One sees the data agrees very well with expectations that $S_0^{-1/2}$ is a linear function of T_g/T in the range $T_g/T=0.46-0.74$. The red line corresponds to the van der Waals model analytic representation [69] $S_0^{-1} = 9(1141.53K/T - 0.5271)^2$, which is employed in the main text to map the hard polymer chain model to its thermal PnBA analog at 1 atm. Inset: Relationship between effective packing fraction from PRISM theory and temperature for PnBA deduced from the mapping procedure [39-41].

C. Dynamic Relaxation of Kuhn Segments and Glass Transition Temperature.

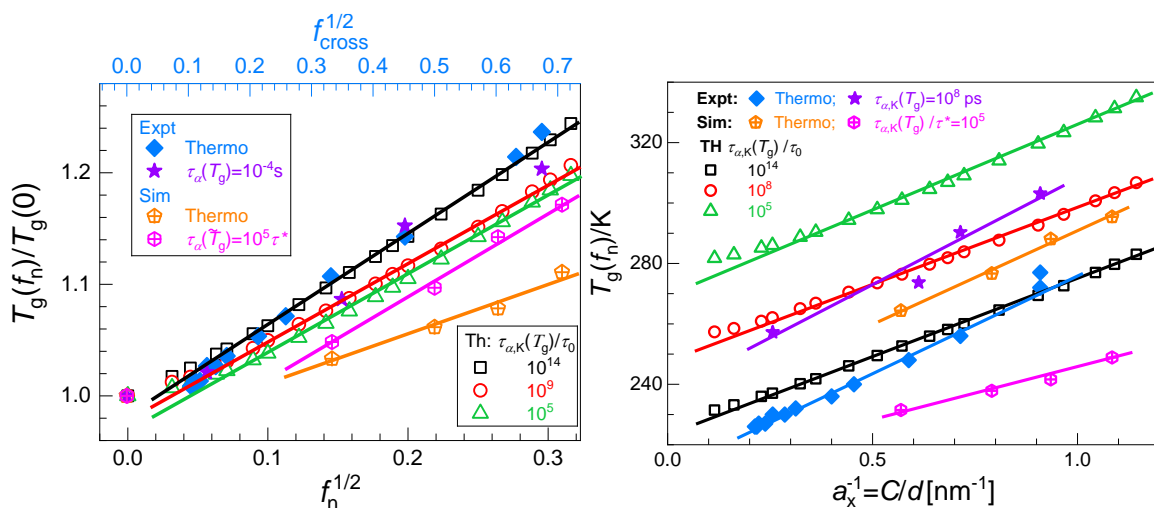


Fig.3. (a) Comparisons between scaled glass transition temperatures from experiment, simulation, and theory ($l_p/\sigma = 1.2$ model) extracted and defined in two ways as indicated (dynamic and

thermodynamic), $T_g(f_n)/T_g(0)$, plotted as a function of the square root of crosslink fraction. The experimental and simulated *crosslink fractions* are taken to be exactly the same and the theory analog obeys $f_n = 0.19f_{\text{cross}}$ [41]. (b) Glass transition temperature $T_g(f_n)$ in Kelvin as a function of inverse mesh size. Experimental and simulation mesh sizes are directly measured where the bond length $l_b = 0.72\text{nm}$ was used in simulation as the length unit [41] while in the theory analysis the mesh size is calculated using $a_x^{-1} = A(f_n/0.19)^{1/2}/\sigma$ with $A=1.94$ (see main text).

We first consider how the degree of crosslinking affects the glass transition temperature $T_g(f_n)$ defined in the theory as when Kuhn segment alpha time reaches a fixed value relevant to a specific experiment or simulation; here we employ $\tau_{\alpha,K}(T_g)/\tau_0 = 10^{14}$, 10^8 , and 10^5 to illustrate our predictions based on a vitrification criterion in the laboratory deeply supercooled, intermediate supercooled, and weakly supercooled (per simulations) regimes, respectively. This issue was studied in our previous publication for the $l_p/\sigma = 4/3$ Koyama model where we found $T_g(f_n)$ grows non-linearly with f_n , but no quantitative relationship was identified.[41] Here, as shown in Fig.3a, we report a *new* discovery of a square-root relationship, $T_g(f_n) \propto f_n^{1/2}$, with only small deviations evident in the very low crosslink density regime. Adoption of different T_g criteria do not change the robustness of this relation. Fig.3a also shows that the previously obtained experimental and simulation $T_g(f_{\text{cross}})$ data also obey well the relation $T_g(f_{\text{cross}}) \propto f_{\text{cross}}^{1/2}$. We note that in our prior joint experiment-simulation-theory study for PnBA based on the $l_p/\sigma = 4/3$ model, the experimental crosslink fraction was given by $f_{\text{cross}} = f_n/0.19$.[41] This prefactor of 0.19 remains unchanged for the present $l_p/\sigma = 1.2$ model, and the numerical scaling factor likely reflects the difference between our model construction based on the neutral pinning idea of coarse-grained polymer model and real crosslinking of chemically complex polymers.

In polymer networks, an alternative variable to the crosslink fraction f_n is the mean geometric mesh size, a_x . In our theory, this quantity does not play any direct role. However, based on its classic definition in experiment and simulation, a_x is proportional to the square root of the

average number of bare beads between two neighboring crosslinks N_x , i.e., $a_x \propto \sigma N_x^{1/2}$, where $f_{\text{cross}} = 1/N_x \equiv n_{\text{crosslink}}/(n_{\text{crosslink}} + n_{\text{monomer}})$. As such, one has $a_x \propto \sigma/f_{\text{cross}}^{1/2}$, and we quantify this connection as $a_x = \sigma/Af_{\text{cross}}^{1/2} = \sigma/A(f_n/0.19)^{1/2}$. Since $A/\sigma = 1/(a_x f_{\text{cross}}^{1/2})$, one can compute A using purely experimental results for a_x and f_{cross} . However, to be consistent with a previous simulation of penetrant diffusion in semi-dilute solutions based in a coarse grained polymer bead model (as we also employ) [57] where $A = 1.94$ was adopted to achieve the best agreement of simulation data with the formula $\log(D_p) \sim (d/a_x)^2$, we a priori fix $A = 1.94$. To check the sensitivity of our theoretical results concerning this choice, we demonstrate below that using $A = 4.0$ does not modify any of our qualitative findings.

Based on $a_x = \sigma/A(f_n/0.19)^{1/2} \propto 1/f_n^{1/2}$ and our above discovery that $T_g(f_n) \propto f_n^{1/2}$, we deduce that $T_g(f_n)$ and $a_x^{-1}(f_n)$ are proportional. In experiment and simulation, the average mesh size a_x can be directly measured [9] instead of using $a_x = \sigma/Af_{\text{cross}}^{1/2}$. Here based on previous experimental results of PnBA for mesh size a_x [9] and glass transition temperature $T_g(f_{\text{cross}})$ [9, 41], and our published $T_g(f_{\text{cross}})$ [41] and a_x estimates from simulations [58], we test the linearity between $T_g(f_n)$ and $a_x^{-1}(f_n)$ in Fig.3b. We find excellent agreement over the entire range of data.

We now consider the predictions of ECNLE theory for the polymer network alpha relaxation time for a choice of aspect ratio (1.2) modestly different than in prior work [41]. Figure 4a shows the foundational results for the nonlocal collective elastic (solid) and local cage (open) barriers as a function of $T_g(f_n)/T$ over a wide range of crosslink densities (covering all ranges that was achieved in experiments [9]) at various fixed temperatures. The theoretical results are plotted based on two very different dynamic T_g criteria appropriate for the deeply and weakly supercooled regimes in the main frame and inset of Fig.4a, respectively. Different choices of vitrification

criterion do not, at zeroth order, change the qualitative finding of a good collapse and shape of the master curves. Of course, quantitatively the barriers cannot be identical, and must be larger at the same $T_g(f_n)/T$ based on defining glass formation with a longer alpha time criterion. For the classic laboratory criterion that the network vitrifies when the alpha time is 100s, the elastic barrier results as a function of $T_g(f_n)/T$ collapse very well over the *entire* T_g/T range for *all* temperatures that corresponds to ~ 16 decades growth of the alpha time. The local cage barriers at different temperatures do not collapse as well, although the deviations are not large. Moreover, we find the local cage barrier grows linearly with $T_g(f_n)/T$ for each fixed temperature, while the elastic barrier grows in a non-linear manner, a feature that has been discussed in great depth previously [41].

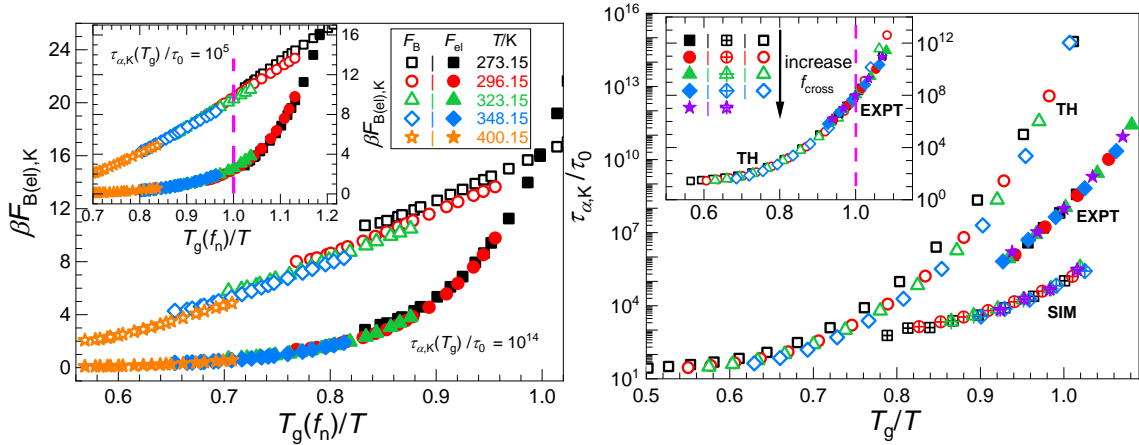


Fig.4. (a) Kuhn segment local cage and collective elastic barriers and (b) mean alpha relaxation time based on different T_g definition criteria as a function of T_g/T over a wide range of crosslink densities for the $l_p/\sigma = 1.2$ model. In (b) the experiment and simulation results are also shown. The T_g criteria in the main frame and inset of (a) are $\tau_{\alpha,K}(T_g)/\tau_0 = 10^{14}$ and 10^5 (using an elementary time scale $\tau_0 \sim 1$ ps per typical viscous liquids), respectively, while for the main frame of (b) they are $\tau_{\alpha,K}(T_g) = 10^8$ ps, $\tau_{\alpha,K}(T_g) = 10^5$ corresponding to ~ 320 ns, and $\tau_{\alpha,K}(T_g)/\tau_0 = 10^{14}$, for experiment, simulation, and theory, respectively, and for the inset of (b) they are the same for both experiment and theory, i.e., $\tau_{\alpha,K}(T_g) = 10^8$ ps or $10^8\tau_0$. Note the variable T_g/T in (a) is crosslink fraction dependent at fixed temperature ($T/K = 273.15, 296.15, 323.15, 348.15, 400.15$, respectively), i.e., $T_g(f_n)$, while that in (b) is temperature at fixed crosslink fraction ($f_n = 0, 0.02, 0.04, \text{ and } 0.1$, respectively). The vertical line in the inset of (a) or (b) represents an estimate of a higher kinetic glass transition temperature, which is far higher than the normal glass transition temperature deduced thermodynamically or dynamically in experiment of ~ 100 seconds.

Given the predicted collapse behavior for the elastic barriers and near collapse of the local cage barriers for different temperatures and crosslink densities, a nontrivial collapse of the total barrier and hence the Kuhn scale alpha times for all temperatures and crosslink densities is expected. Figure 4b verifies this is the case for the $l_p/\sigma = 1.2$ model. This behavior provides a theoretical basis for the collapsed Angell plots observed in experiment and simulation, as shown in the main frame of Fig.4b. Finally, we emphasize that the theoretical results in Fig.4 provide foundational input to the SCCH theory since the penetrant dynamic free energy is coupled with the polymer network dynamic free energy [34, 42, 43].

III. SCCH Theory in Crosslinked Polymer Networks

A. Theoretical Background for Penetrant Dynamics

We now briefly recall the key physical elements of the SCCH theory[34, 42, 43, 45] for the mean penetrant hopping time which describes an activated process (see the corresponding penetrant dynamic free energy in the left panel of Fig.5) which is self-consistently coupled with an activated dynamic “facilitation displacement” of polymer segments determined by the Kuhn segment dynamic free energy (see the middle panel of Fig.5). Crucially, the penetrant dynamic free energy depends on *both* its displacement *and* that of the Kuhn segment (r_p and r_k , respectively). The mathematical formulation of SCCH theory has been discussed in great detail previously for a dilute penetrant in a hard sphere fluid[42, 43, 45] and in a polymer melt[34]. The derivative of the penetrant dynamic free energy in polymer melts is given as [34]:

$$\frac{\partial \beta F_{\text{dyn,p}}(r_p, r_k)}{\partial r_p} = -\frac{3}{r_p} + \frac{r_p}{3} \int \frac{d\mathbf{q}}{(2\pi)^3} q^2 \rho C_{\text{mp}}^2(q) S_{\text{mm}}(q) e^{-q^2 r_p^2/6} e^{-q^2 r_k^2 \omega_K(q)/6 S_{\text{mm}}(q)} \quad (5)$$

where ρ is the number density of matrix interaction sites or beads (see Fig.1), $C_{mp}(q)$ is the Fourier transform of the penetrant-polymer site-site direct correlation function, $S_{mm}(q)$ is the Fourier space static collective structure factor of the polymer network, and $\omega_K(q)$ is the intramolecular structure factor of the elementary Kuhn segment that in Eq.(5) (it can be set to unity without significantly changing the numerical predictions [34]). The subscript “m” represents the elementary bead or site level (see the left panel of Fig.1) description of the polymer and is employed to distinguish it from the Kuhn segment scale (denoted by the subscript “K”). Based on the pinned bead model of polymer crosslinks[41], Eq.(5) for polymer melt is modified as:

$$\frac{\partial \beta F_{\text{dyn,p}}(r_p, r_K)}{\partial r_p} = -\frac{3}{r_p} + \frac{r_p}{3} \int \frac{d\mathbf{q}}{(2\pi)^3} q^2 C_{mp}^2(q) e^{-q^2 r_p^2/6} \times [S_{uu}(q, r_{Ku}) + S_{nn}(q, r_{Ku}) + S_{un}(q, r_{Ku}) + S_{nu}(q, r_{Ku})] \quad (6)$$

The presence of pinned segments enters via the form of the collective partial Debye-Waller factors of the polymer matrix, $S_{\alpha\beta}(q, r_{Ku})$, which differs from a melt of fully mobile segments as previously derived and discussed []. We additionally note that the subscript Ku refers to the mobile Kuhn segments, and the subscripts u and n indicate unpinned and pinned sites, respectively.

To render SCCH theory predictive and tractable, the degree of Kuhn segment dynamic displacement that facilitates the penetrant hopping event is described by introducing a single trajectory coupling variable, γ , defined as: $r_{Ku}(\gamma) = r_{\text{loc,Ku}} + (r_p - r_{\text{loc,p}})/\gamma$. [34] The “pinned” Kuhn segments (crosslinkers) are also allowed to vibrate locally with an amplitude set by the predicted localization length of unpinned Kuhn segments, i.e., $r_{\text{loc,Kn}} = r_{\text{loc,Ku}}$. The parameter γ is determined based on enforcing a *temporal self-consistency* condition[34, 42, 43]: $\tau_{\text{hop,p}}(\gamma) = \tau_{\text{dis,K}}(\Delta r_{\text{Ku,c}}(\gamma))$, where $\Delta r_{\text{Ku,c}}(\gamma) = \Delta r_p(\gamma)/\gamma$ and both $\tau_{\text{hop,p}}(\gamma)$ and $\tau_{\text{dis,K}}(\Delta r_{\text{Ku,c}}(\gamma))$ are computed using Kramers theory [66, 67] as sketched in section II. Solving the self-consistency condition numerically yields γ

which depends on all control parameters of the problem. Using it, one can then compute the penetrant alpha time as $\tau_{\alpha,p} = \tau_{s,p} + \tau_{\text{hop},p}$, where $\tau_{s,p} = d^2/D_{s,p}$ is the characteristic elementary short-time scale for the penetrant given elsewhere [34, 42]. As in ECNLE theory of one-component liquids, at high enough matrix packing fractions the penetrant jump length can become (depending on penetrant size) sufficiently large that a collective elastic distortion of matrix particles outside the cage region is required to allow the penetrant to hop.[34, 42, 43] This physics enters via a common elastic barrier ($F_{\text{el},p} = F_{\text{el,Ku,c}}$) in the computation of the timescales $\tau_{\text{hop},p}(\gamma)$ and $\tau_{\text{dis,K}}(\Delta r_{\text{Ku,c}}(\gamma))$. The elastic barrier is determined following the same ideas and methods employed for Kuhn segment in the pure polymer system as discussed above and elsewhere, with the result previously derived as: $\beta F_{\text{el},p} \approx 2\pi(1-f_n)r_{\text{cage,p}}^3\Delta r_{\text{eff,p}}^2\rho_K K_{0,K}$ where $\Delta r_{\text{eff,p}}(\gamma) = 3\Delta r_{\text{Ku,c}}^2(\gamma)/32r_{\text{cage,p}}$, $r_{\text{cage,p}} = r_{\text{min,mp}}(N_K^{1/3}\sigma + d)/(d + \sigma)$, and $r_{\text{min,mp}}$ is the cage radius corresponding to the first minimum of cross radial distribution function $g_{\text{mp}}(r)$. [34, 41] Everywhere below the notation F_{el} (F_B) is employed to indicate the penetrant elastic (local cage) barrier.

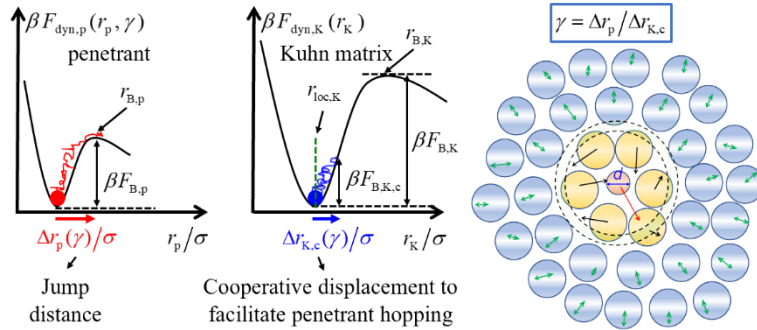


Fig.5. Schematic of the dynamic free energies for the coupled penetrant (left) and Kuhn segment (middle) displacements in SCCH theory. The trajectory level matrix facilitation of penetrant hopping is formulated based on the simplifying concept of a dimensionless dynamic coupling parameter, γ , defined as the ratio of the penetrant jump distance $\Delta r_p(\gamma)$ to the facilitating displacement of the matrix Kuhn segments, $\Delta r_{K,c}(\gamma)$. Relevant length and energy scales are indicated. Right panel: Schematic of the physical ideas of SCCH theory for a single smaller spherical penetrant in a bulk liquid of spheres. The image shows the matrix as disconnected spheres solely for visual clarity and is literally relevant only for the hard sphere mixture model [42, 43].

This completes our brief review of the construction of SCCH theory that includes crosslinking. From knowledge of the coupling parameter, penetrant dynamic free energy, and its local cage and elastic barriers, the SCCH theory then predicts the mean penetrant alpha time, $\tau_{\alpha,p}$, as a function of size ratio, polymer packing fraction or temperature, crosslink fraction, etc.

As discussed in the Introduction, we will apply the theory motivated by a recent experimental study of the relaxation and diffusivity of BTBP in PnBA networks [9]. Modeling BTBP as a sphere, its effective hard sphere diameter is 1.12nm. For the adopted $l_p/\sigma = 1.2$ Koyama model $\sigma=1.23$ nm, while for the $l_p/\sigma = 4/3$ model one has $\sigma=1.03$ nm, thereby yielding a penetrant-to-matrix size ratio of order unity, $d/\sigma=0.91$ and 1.09, respectively.

B. Crosslink Fraction Dependence of Jump Displacements and Associated Properties

In SCCH theory[34], the penetrant jump distance and the facilitation displacement of Kuhn segments are very important for the activated penetrant hopping event since they (i) directly enter calculation of the penetrant elastic barrier, and (ii) the difference between displacements of a Kuhn segment *at* the penetrant and polymer Kuhn segment alpha times provides a mechanistic picture of the degree of trajectory level coupling between the penetrant and Kuhn segment alpha processes. Thus, we first consider these quantities.

Both increasing crosslink fraction and decreasing temperature induces a significant increase of the penetrant and Kuhn segment alpha times. This results in an increased jump distance of both the penetrants and Kuhn segments, as shown in Figs.6a and 6b, respectively. The coupling between penetrant and Kuhn segment activated displacements at the penetrant alpha time corresponds to a facilitation displacement $\Delta r_{Ku,c}$ of a Kuhn segment, which grows with crosslink density or cooling (longer alpha time) as shown in Fig.6b. We note the crosslinking dependence of $\Delta r_{Ku,c}$ is weaker than its temperature dependence, which differs from that of Δr_p and Δr_{Ku} where

both the temperature and crosslinking dependences are significant. We also find that the crosslink density dependence of Δr_p is nearly unchanged with increasing the temperature, i.e., calculations of $\Delta r_p(f_n) - \Delta r_p(0)$ collapse (vertical shift of the data in Fig.6a) for different fixed temperatures (not shown).

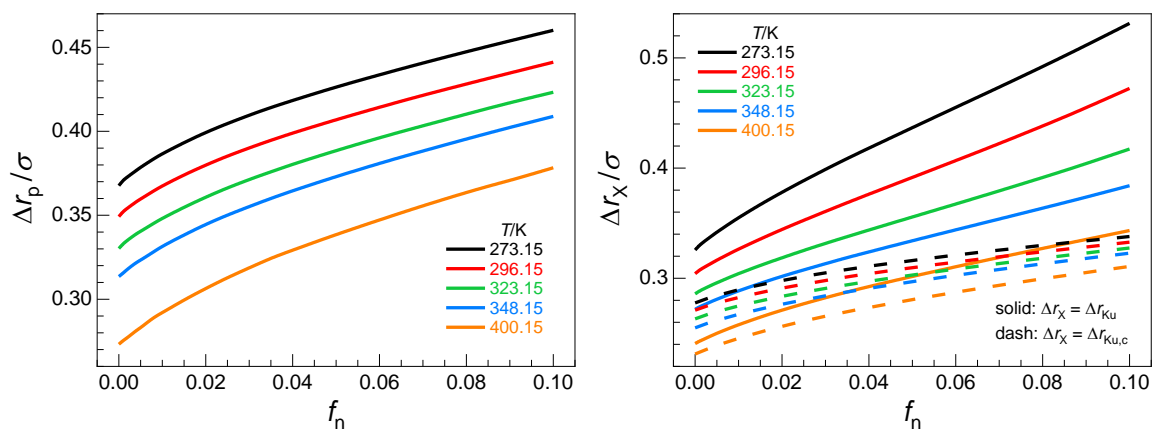


Fig.6. Jump distance of (a) the penetrant, Δr_p and (b) mobile Kuhn segment (solid curves), Δr_{Ku} , in units of σ at their corresponding alpha time scales as a function of crosslink fraction for a wide range of temperatures. The facilitation displacement of unpinned Kuhn segments, $\Delta r_{Ku,c}$, at the penetrant alpha time scale is shown in (b) as dashed curves. The similarity of the absolute magnitude of the penetrant and unpinned Kuhn segment jump distances reflects the strong coupling of their motions as a consequence of the very similar penetrant and Kuhn segment sizes.

Fig.6b also shows that the absolute value of $\Delta r_{Ku,c}$ (corresponding to the penetrant alpha time scale) is much lower than that of Δr_{Ku} (corresponding to the Kuhn segment alpha time scale), and the difference increases significantly with degree of effective supercooling (lowering temperature or increasing crosslink fraction). This suggests that the dynamical coupling between penetrant and polymer matrix weakens at lower temperatures and higher crosslink densities. For the highest temperature $T = 400K$ and lower crosslink density regime shown in Fig.6b, the crosslink dependence of $\Delta r_{Ku,c}$ is very similar to that of Δr_{Ku} , corresponding to a relatively stronger coupling between the alpha relaxations of the penetrant and polymer matrix.

One can also see from Fig.6b that the absolute value of the Kuhn segment facilitation displacement is not much smaller than the location of its barrier (Kuhn segment jump distance).

This implies there is a strong coupling between penetrant and Kuhn segment alpha relaxations and suggests the dynamic coupling parameters, γ , defined as the ratio of penetrant jump distance $\Delta r_p(\gamma)$ to the facilitating Kuhn segment displacement $\Delta r_{Ku,c}(\gamma)$, should not be much larger than unity. Figure 7a shows this to be the case. The smaller γ is, the larger is the dynamic coupling of activated penetrant and polymer matrix displacements. Figure 7a also shows that the coupling decreases with cooling and crosslink fraction as physically expected, but the dependences are weak. The reason is that the penetrant jump distance has a significant temperature dependence while that of Kuhn segment facilitation displacement is more limited (per Figs.6a and 6b), while both their crosslinking dependences are rather weak. Since the temporal self-consistency condition is $\tau_{hop,p}(\gamma) = \tau_{dis,K}(\Delta r_{K,c}(\gamma))$ with $F_{el,p} = F_{el,K,c}$, the coupling parameter γ encodes dynamical displacement physics associated only with local caging. Therefore, variation of γ with crosslink fraction is physically intuitive, even in the large crosslink fraction regime it is nearly constant.

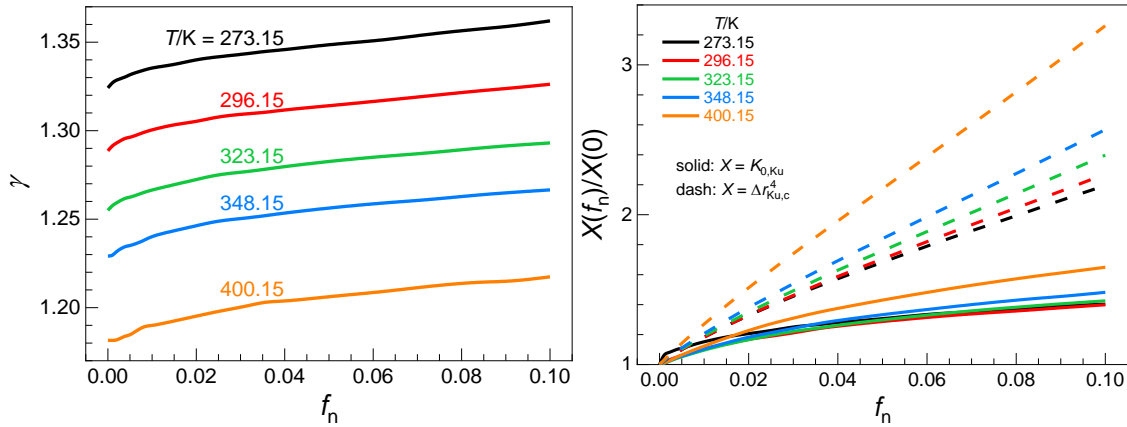


Fig.7. (a) Self-consistently determined dynamic coupling parameter, $\gamma \equiv \Delta r_p / \Delta r_{Ku,c}$, as a function of crosslink fraction at various temperatures. (b) Relative importance of the key factors $\Delta r_{Ku,c}^4$ (dash) and $K_{0,Ku}$ (solid) reduced by their values at zero crosslink fraction that enter the penetrant elastic barrier as a function of crosslink fraction at various temperatures.

Finally, in Fig.7b we compare the relative importance of the two key factors $\Delta r_{Ku,c}^4$ and $K_{0,Ku}$ that enter the calculation of penetrant elastic barrier. The harmonic curvature $K_{0,Ku}$ (proportional to the inverse dynamic localization length squared) weakly increases with cooling

and crosslink fraction, with $K_{0, Ku}(f_n)/K_{0, Ku}(0)$ varying only from ~ 1.0 - 1.4 for all ranges of temperature and crosslink fractions studied. For pure hard sphere fluids, increases of the localized state spring constant with packing fraction is the most important origin for the corresponding increase of the elastic barrier^[35]. However, for networks, Fig.7b shows that as crosslink fraction increases, the jump distance contribution $\Delta r_{Ku,c}^4$ dominates the change of elastic barrier. The reason is that introducing crosslinking increases the penetrant hopping time, and hence penetrants can displace significantly more corresponding to a larger jump distance.

IV. Penetrant Alpha Relaxation Time

We now consider theoretical predictions for quantities that are directly measurable in experiment and simulation, specifically the penetrant alpha relaxation time in this section. In the context of empirical experimental and simulation data^[9, 56, 57], one can consider two different ways of displaying its dependence on a control parameter depending on which physical perspective one thinks is the primary origin of effect of network crosslinking on penetrant motion: crosslink dependent changes of segmental dynamics (i.e., activated glassy physics) versus entropic mesh confinement. In this section we only pursue an objective empirical analysis based on plotting the theoretical data for the penetrant alpha time in two different ways. Of course, we know the physics in SCCH theory is *all* about activated hopping dynamics. Our goal is to test whether a “degeneracy of interpretation” of the theoretical results might exist due to the discovered connection between T_g and mesh size discussed in section II. This exercise does not answer the question whether the physics of penetrant diffusion is dominated by segmental scale glassy effect or entropic mesh confinement, the answer to which must depend to some extent on T_g/T , crosslink density, and penetrant-to-matrix size ratio. This question is explored in section VI, and in our companion simulation article.

As a preview of the combined insights gleaned from the results in the remainder of our present theoretical work and the complementary simulations, we find for the penetrant sizes studied that although the crosslink fraction dependent (but temperature *independent*) entropic mesh confinement does affect penetrant diffusivity, it is an increasingly secondary (and ultimately very minor) effect as the temperature is lowered in the supercooled regime of interest compared to the coupling of penetrant hopping to the temperature and crosslink fraction dependent activated barrier hopping associated with glassy dynamics.

A. Crosslinking Modified Segmental Dynamics Perspective

Figure 8 shows results for the inverse penetrant mean alpha time as a function of the temperature scaled glass transition temperature, $T_g(f_n)/T$, over a wide range of crosslink fractions at various fixed values of temperature. The results are presented based on a typical laboratory timescale criterion for vitrification (main panel) and a much smaller simulation-like timescale criterion (inset). The predicted behaviors are very similar for the two criteria. For each fixed temperature, the penetrant alpha relaxation time $\tau_{\alpha,p}/\tau_0$ ($\tau_0 \sim 1$ ps per a typical viscous liquid) is predicted to increase exponentially with $T_g(f_n)$, in the spirit of an ‘‘Arrhenius-like’’ law. Moreover, we observe that the corresponding apparent activation energy [defined as the slope of $\log(\tau_{\alpha,p}/\tau_0)$ versus $T_g(f_n)/T$, see Table 1] and the absolute value of $\tau_0/\tau_{\alpha,p}$ decreases and increases with temperature, respectively. Overall, results for different temperatures are rather well collapsed. There is a weak trend of lower penetrant hopping rate upon cooling, which is more prominent in the main frame that is relevant to laboratory experiments. As discussed in detail below, the reason for this difference, *and* for the roughly Arrhenius-like form of the penetrant alpha time, is the relative unimportance of the elastic barrier compared to its local cage analog. The latter is

quantitatively more true in the simulation based choice for T_g results which do not probe the deeply supercooled regime.

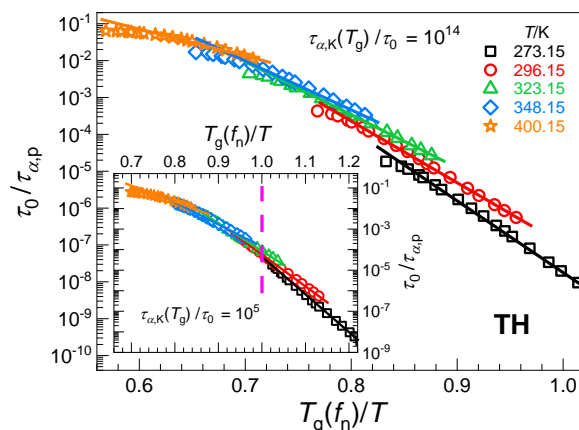


Fig.8. Penetrant inverse mean alpha time based on SCCH theory as a function of $T_g(f_n)/T$ at various fixed temperatures for vitrification criteria $\tau_{\alpha,K}(T_g)/\tau_0 = 10^{14}$ (main) and 10^5 (inset). The vertical line in the inset is an estimate of a higher kinetic glass transition temperature, which corresponds to a simulation criterion of vitrification that delivers a glass transition temperature far higher than its laboratory based analog.

Table 1. Slope of the logarithm of the penetrant alpha time versus T_g/T or C plot for various fixed temperatures and T_g criteria where $A=1.94$ is adopted in theoretical evaluation of C .

T/K	T_g criterion	273	296	323	348	400
$\log(\tau_{\alpha,p}/\tau_0)$ vs T_g/T	10^5	18.4	15.3	13.5	11.7	7.3
$\log(\tau_{\alpha,p}/\tau_0)$ vs T_g/T	10^{14}	19.4	17.1	14.8	12.8	7.5
$\log(1/D_p)$ vs T_g/T	10^5	26.2	23.7	22.2	20.6	17.2
$\log(1/D_p)$ vs T_g/T	10^{14}	28.0	25.6	24.2	22.3	19.2
$\log(\tau_{\alpha,p}/\tau_0)$ vs C		3.3	2.8	2.2	1.8	0.77
$\log(1/D_p)$ vs C		4.5	3.8	3.2	2.8	2.1

SCCH theory can provide the physical mechanism to understand how crosslinking modifies the penetrant alpha relaxation process by carefully examining the penetrant local cage and collective elastic barriers. Figure 9 presents theoretical results for these quantities in an Angell-

like representation, where the dynamic $T_g(f_n)$ criterion appropriate for the deeply supercooled regime of highest experimental relevance is adopted. For all fixed temperatures studied, the elastic barriers are far smaller than the local cage barriers. There are several reasons for this: (i) for polymer systems, the relative importance of the elastic barrier is modestly weaker because of the influence of chain connectivity [37,38], and (ii) the penetrant size is relatively small which is known to induce significant decoupling between the penetrant and matrix dynamics and a lower elastic barrier. Figure 9 also shows that the elastic barrier increases more slowly with $T_g(f_n)/T$ relative to that of local cage barrier. Hence, the total penetrant barrier and its growth with $T_g(f_n)/T$ is largely dominated by the local cage barrier, and for $T_g(f_n)/T \leq 1$ it is more so for the simulation timescale vitrification criterion (inset) than its laboratory analog.

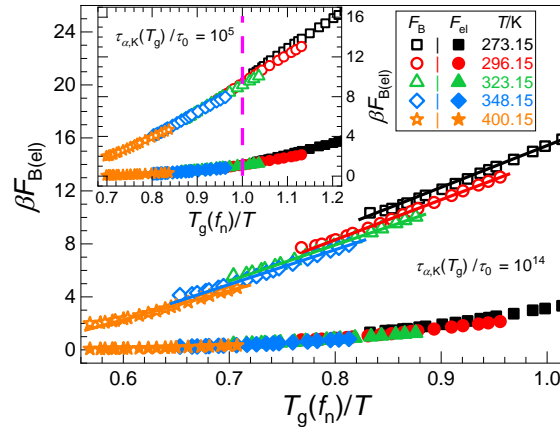


Fig.9. Penetrant local cage (open) and collective elastic (solid) barriers as a function of $T_g(f_n)/T$ at various temperatures with the T_g criteria in main frame and inset corresponding to $\tau_{\alpha,K}(T_g)/\tau_0 = 10^{14}$ and 10^5 , respectively. The vertical line in the inset represents an estimate of a higher kinetic glass transition temperature corresponding to a typical simulation criterion.

More insight is obtained by comparing Figs.9 and 4a, which shows that the penetrant local cage barrier is comparable to its Kuhn segment analog, as expected from the predicted strong coupling between activated hopping of the penetrant and Kuhn segment displacements as manifested in the close to unity value of the coupling parameter γ in Fig.7a. On the other hand,

the penetrant elastic barrier is far smaller than its Kuhn segment analog because its facilitation displacement is much smaller than the jump distance associated with the pure network alpha relaxation. The latter result can be seen from Fig.6b and the fact that the jump distance enters the penetrant elastic barrier as the 4th fourth power (see section III).

The local cage barrier varies linearly with $T_g(f_n)/T$ which is the same behavior predicted for the Kuhn segment (Fig.4a). The fact that this linearity is sufficiently well obeyed over the entire range of T_g/T is why an exponential relationship between alpha time and $T_g(f_n)/T$ is found in Fig.8. Note also from Figs.4a and 9 that at fixed $T_g(f_n)/T$ the local cage barriers for both the penetrant and Kuhn segments are slightly larger at lower temperature. This implies that normal glass-like physics effects play an important role in determining the temperature dependence of the penetrant alpha time, which is intensified in the high crosslink density regime. This behavior also explains why the apparent activation energy (Table 1) increases as temperature decreases.

B. Confinement Mesh Perspective

We now explore the extent to which the SCCH theory results for the penetrant alpha time can be *empirically* interpreted in a purely confinement mesh scenario, $D_p \propto \exp(-BC^2)/C$ or $D_p \propto \exp(-EC)$, per Eqs (2) and (3). Specifically, we ask if the crosslink fraction dependent penetrant alpha time data can be “correlated” or “described” as: $1/\tau_{\alpha,p} \propto \exp[-(B-1)C^2]$ and/or $1/\tau_{\alpha,p} \propto \exp[-(E-b')C]$. Obviously, the entropic mesh perspective cannot account for explicit temperature dependences of the theoretical penetrant alpha time.

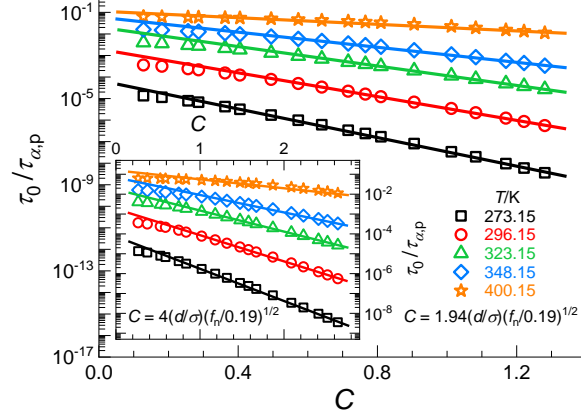


Fig.10. Inverse penetrant mean alpha time $\tau_0/\tau_{\alpha,p}$ as a function of the confinement parameter at various fixed temperatures. The main frame uses $C = 1.94(d/\sigma)(f_n/0.19)^{1/2}$, while the inset adopts $C = 4(d/\sigma)(f_n/0.19)^{1/2}$.

Figure 10 plots in a log-linear manner the theoretical penetrant relaxation rate as a function of confinement parameter $C = d/a_x$ over a wide range of crosslink densities and temperatures. A linear relationship is observed, albeit with a slope that decreases strongly with temperature. The latter trend is due to activated glassy dynamics effects, and is inconsistent with a literal [55-57] entropic confinement mesh picture (see Table 1). Thus, as a cautionary comment, if simulation or experimental data is taken at only one temperature or over a narrow range, one could incorrectly conclude that the confinement mesh idea is “verified”. Indeed, the slope changes documented in Table 1 prove the importance of T -dependent physics in crosslinked polymer networks, and necessarily implies the rate of increase of the alpha time with T_g/T is significantly larger than that with C . Physically the reason is simply the very different rate of change of T_g and C with crosslink density f_n . As discussed in section II, $T_g(f_n)$ is proportional to inverse mesh size a_x^{-1} and hence $C(f_n)$ for a fixed penetrant size and different vitrification criteria, which is the non-causal reason the curves in Fig.10 are linearized. Our conclusions remain robust with varying the constant A in defining the confinement parameter, as shown in the inset of Fig.10 where $A = 4.0$ is adopted.

We also tested whether a linear relationship between $\log(\tau_{\alpha,p}/\tau_0)$ and C^2 can empirically “work” (not shown), i.e., $1/\tau_{\alpha,p} \sim \exp[-(B - 1)C^2]$, and find it is also a reasonable description in the limited C regime examined in Fig.10. However, for large enough C , SCCH theory predicts that the exponential relationship $1/\tau_{\alpha,p} \sim \exp[-(E - b')C]$ will break down since the elastic barrier of penetrant becomes more and more important and it does not grow linearly with confinement parameter but rather quadratically (see Fig.9). Simulation tests of the relations $1/\tau_{\alpha,p} \propto \exp[-(B - 1)C^2]$ and $1/\tau_{\alpha,p} \propto \exp[-(E - b')C]$ are reported in our companion paper, and good agreement between theory and simulation is found.^[58]

V. Decoupling Ratio of Penetrant and Network Alpha Times

As previously studied using SCCH theory for hard sphere mixtures ^[42, 43] and dilute spherical penetrants in polymer melts ^[34], the ratio of the penetrant to Kuhn segment alpha times can be predicted which quantifies the degree of “dynamic decoupling”, a quantity that is measurable in simulations and experiments. This quantity is especially sensitive to collective elasticity given the hopping of penetrants and Kuhn segments couples to this longer range effect generally to very extents. In prior work ^[34, 42], the decoupling time ratio, $\tau_{\alpha,p}/\tau_{\alpha,K}$, was plotted as a function of packing fraction, and found to initially increase very slightly with matrix packing fraction in the lower packing fraction regime (corresponding to high temperature where barriers are low and the timescale of the short time dynamical process, $\tau_{s,p}$ and $\tau_{s,K}$, matter), and then sharply decrease with further increase of packing fraction indicating a strong decoupling between penetrant and matrix activated dynamics when the penetrant and matrix barriers become larger and dominate the alpha relaxation times. The crucial physical effect is the very different rate at which the penetrant and matrix elastic barriers grow with increasing packing fraction or decreasing

temperature, a difference significantly larger than that for their local cage barrier analogs (see results in Fig.4a and Fig.9).

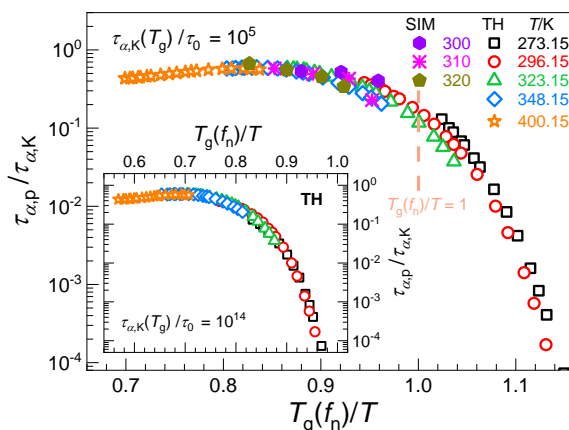


Fig.11. Decoupling time ratio as a function of $T_g(f_n)/T$ for various values of crosslink density f_n using $\tau_{\alpha,K}(T_g)/\tau_0 = 10^5$ (main) and 10^{14} (inset) T_g criteria and for four temperatures in theory and for three temperatures for the $d/\sigma = 1.0$ simulations [58]. The simulation data of mean alpha relaxation times are based on the 1/e decay definition criterion, and the time ratio is vertically shifted up by a factor of 480 in the main panel for comparison of their functional form with the theory results. The vertical line in the main frame represents an estimate of a higher kinetic glass transition temperature based on the simulation vitrification criterion.

The inset of Figure 11 shows theoretical predictions for the decoupling time ratio plotted versus $T_g(f_n)/T$ over a wide range of $T_g(f_n)/T$ from the rubbery regime, through the deeply supercooled regime, to the laboratory kinetic glass transition. For the four lower temperatures studied (273, 296, 323, 348 K) the time ratio decreases monotonically with the effective degree of supercooling parameter, $T_g(f_n)/T$. In contrast, at high temperature (400 K) where barriers are relatively small and only the local cage barrier is non-negligible, a nearly constant (weakly decreasing) behavior is predicted. Overall, for all five temperatures (which span a change of the polymer network alpha time of ~14 decades), a nonmonotonic behavior is found, qualitatively consistent with the previous predictions for other systems [34, 42]. A new finding is that for all temperatures and crosslink densities, the decoupling time ratio tends to collapse in $T_g(f_n)/T$ space with only slight deviations visible in the high $T_g(f_n)/T$ regime. We hope future experiments can

test our results in the deeply supercooled regime where a significant decrease of the decoupling ratio is predicted.

We have verified that all of the above findings remain unchanged if a different T_g criterion is adopted. The main frame of Fig.11 shows an example based on a vitrification criterion relevant to simulations. For the three temperatures simulated (300, 310, and 320 K based on the calibrated PnBA coarse-grained network model employed) the decoupling time ratio slightly decreases monotonically, and the data is in good agreement with our prediction in this weakly supercooled regime. We hope future simulations can better test the predicted weakly non-monotonic behavior with T and probe lower temperatures.

VI. Penetrant Diffusion Constant

A. Introductory Comments and High-Level Picture

We now consider the predictions of Eqs.(2) and (3) which combine in a simple multiplicative manner the activated physics (at the level of mean alpha relaxation times) of SCCH theory with the entropic mesh confinement effect. We showed in section IV that the glass physics based theoretical local hopping rate can be *empirically* described using the mathematical relations of the entropic mesh models formulated solely in terms of the mesh confinement variable C ($1/\tau_{\alpha,p} \propto \exp [-(B - 1)C^2]$ and $1/\tau_{\alpha,p} \propto \exp[-(E - b')C]$). Thus, logically, introducing the latter mechanism into Eqs. (2) or (3) [i.e., $X(C) = \exp(-C^2)/C$ or $X(C) = \exp(-b'C)$] cannot change the basic *form* of our results for how crosslink fraction modifies the diffusion constant *if* expressed in terms of C .

Now, adopting Eqs.(2) or (3) for the penetrant diffusion constant, our theoretical finding that the penetrant alpha relaxation rate can be empirically described in a mesh confinement parameter framework implies it will be very difficult or impossible to dissect how important the

factors $1/\tau_{\alpha,p}$ and $X(C)$ are *at fixed temperature* from experimental or simulation data. Of course, insight can be obtained from by studying the temperature dependence of the penetrant relaxation time and diffusion constant. Here, in the next subsection we consider a quantitative comparison of the theoretical predictions with and without the mesh confinement effect. In addition, as discussed in more detail in our companion simulation paper^[58], reasonable, albeit not in general quantitative, agreement between SCCH theory and simulation for both the crosslink fraction and temperature dependences of the penetrant diffusion constant based on Eq.(2) is found, which systematically *improves* as the polymer network becomes increasingly supercooled. The latter trend is expected given mesh confinement is of entropic origin in contrast to the crosslinking-induced prolongation of segmental relaxation which becomes increasingly more important in colder polymer networks.

Some of the key deductions reported in our companion simulation paper ^[58] can also be drawn from the purely theoretical effective slope data in Table 1. One sees that under the same conditions, the effective slope determined from the diffusion constant is *larger* than that determined from the inverse alpha time, consistent with the existence of an additional mesh confinement contribution. Of course, in general, one a priori expects that the relative importance of glassy physics and mesh confinement depends on both temperature and penetrant size, with the latter (former) expected to dominate at sufficiently high (low) temperatures. Importantly, “high” and “low” depends on penetrant size since the degree of coupling of penetrant activated hopping with the polymer network dynamics depends on the penetrant size relative to the size of the polymer monomer or Kuhn segment. An additional generic physical effect in pure glass-forming liquids is “dynamic heterogeneity” (DH) which induces a distribution of activation barriers and hopping times in the lower temperature supercooled regime, and an associated decoupling of diffusivity and relaxation corresponding to a weaker temperature dependence of the self-diffusion

constant than the alpha time. The consequences of such a DH effect is not well established for penetrant dynamics, but it is expected to be present at some level, and would go in the opposite direction of the entropic mesh confinement induced slowing down of diffusion relative to relaxation. The version of ECNLE and SCCH theories employed in this article focus solely on the mean barriers and relaxation times, and do not consider this type of DH. Thus, its absence can lead to deviations of some theoretical predictions with simulation at lower temperatures and especially for smaller penetrants, as confirmed in our companion paper.^[58] On the other hand, at higher temperatures and/or for large penetrants where DH effects are either intrinsically small or are sufficiently averaged over, respectively, one expects better agreement between theory and simulation, as we have verified.^[58]

We note that the ECNLE theory for the alpha relaxation in 1-component glass-forming atomic, molecular and polymer liquids has been extended to include DH via a distribution of collective elastic barriers and relaxation times^[71, 72]. It captures well the Stokes-Einstein breakdown or diffusion-relaxation decoupling and temperature-dependent stretched exponential relaxation in molecular liquids, and also the nonuniversal failure of time-temperature-superposition in polymer melts corresponding to the decoupling of the temperature dependences of the segmental alpha and chain scale end-to-end relaxation times. The ideas developed in these prior works can be extended to the penetrant dynamics problem in the framework of SCCH theory.

Finally, we emphasize that given the structure of Eq.(2), penetrant diffusivity will be slowed down more with crosslinking than that of penetrant alpha relaxation. This represents a qualitatively distinct form of “decoupling” of penetrant mass transport and relaxation in polymer networks compared to one-component glass forming liquids, as discussed above.

B. Quantitative Theoretical Predictions

Theoretical results are presented in Fig.12 for the penetrant diffusion constant based on $D_p \equiv \frac{d^2}{\tau_{\alpha,p}} \exp(-C^2)/C$ plotted as a function of $T_g(f_n)/T$ over a wide range of crosslink fractions for T_g criteria of $\tau_{\alpha,K}(T_g)/\tau_0 = 10^{14}$ (main) and 10^5 (inset). As found for the penetrant inverse alpha time in Fig.8, and as expected based on our insights that connect $T_g(f_n)$ and C discussed in section II, we predict (i) the diffusion constant also varies exponentially with $T_g(f_n)$ with a linearity even better than that shown in Fig.8, and (ii) the slope of the logarithm of diffusion constant versus $T_g(f_n)/T$ plot decreases with heating. However, the absolute value of diffusion constants at fixed $T_g(f_n)/T$ weakly decreases with temperature, opposite to our findings for inverse alpha time (see Fig.8). This difference is a rather subtle 2nd order effect, but it is an objective signature of the importance of mesh confinement for the diffusion constant that is amenable to experimental and simulation tests. Hence, we now discuss its origin in more detail.

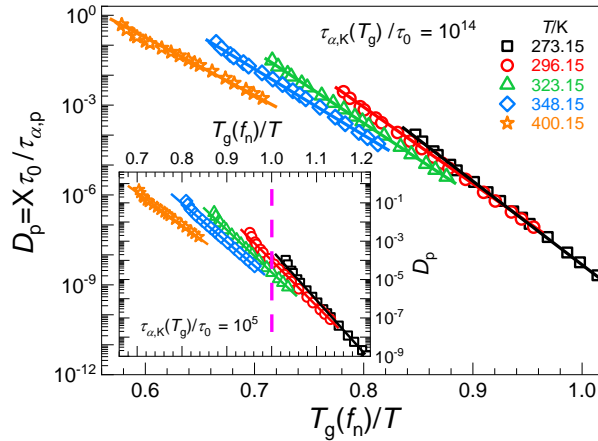


Fig.12. Penetrant diffusion constant as a function of $T_g(f_n)/T$ at various temperatures for vitrification criteria of $\tau_{\alpha,K}(T_g)/\tau_0 = 10^{14}$ (main) and $\tau_{\alpha,K}(T_g)/\tau_0 = 10^5$ (inset). The vertical line in the inset represents an estimate of a higher kinetic glass transition temperature that corresponds to a simulation-like vitrification criterion.

Per Eq.(2), the difference between the diffusion constant and inverse alpha time is proportional to $\exp(-C^2)/C$. At fixed $T_g(f_n)/T$, a lower T corresponds to a lower $T_g(f_n)$, fewer crosslinks, a larger mesh, and hence a smaller confinement parameter C . This trend results in an

increase of the diffusion constant with cooling in the representation of Fig.12. In contrast, the inverse alpha time decreases with cooling, resulting in the opposite trend with T in Fig.8.

The corresponding slope (proportional to an effective activation barrier) for the logarithm of the diffusion constant versus $T_g(f_{\text{cross}})/T$ based on SCCH theory is shown in Table 1. Relative to its analog for the inverse penetrant alpha time, its absolute value increases significantly to a degree that depends on temperature, T_g criterion, and the chemistry-specific parameter A that enters the quantification of the confinement parameter C . In our companion simulation paper [58], we show that by using the commonly adopted $1/e$ decay criterion of the time correlation functions employed to define the penetrant alpha relaxation time, the degree of DH is small, and it is thus appropriate to quantitatively compare such simulation results to our theory. We find from simulation that the effective slope change with temperature for $\frac{d}{\sigma} = 1$ is significant for the inverse alpha time (from 8.0 to 2.6), but moderate/minimal for the diffusion constant (from 9.5 to 6.1). In the present theory, the slope change for both the inverse alpha time and diffusion constant with temperature is moderate (Table 1). We suspect this difference arises from the approximate nature of Eq.(2) with $X(C) = \exp(-C^2)/C$ which reflects our simple ansatz for how to combine glassy activated physics and mesh confinement to predict diffusivity. Indeed, our complementary simulations[58] do find modest deviations from the simple formula $D_p \sim \exp(-C^2)/C\tau_{\alpha,p}$, though they decrease with cooling as the glass physics effects become relatively more important. Both theory and simulation[58] find the slope change with temperature for the alpha time is significantly larger than that for the diffusion constant, emphasizing the additional crosslinking effect on penetrant diffusion beyond its coupling with the activated segmental relaxation process.

As mentioned in section VIA, if $D_p \sim \exp(-C^2)/C\tau_{\alpha,p}$ is qualitatively correct then the diffusion constant will decrease more rapidly with $T_g(f_n)/T$ than the penetrant alpha time increases,

opposite to “normal” Stokes-Einstein relation failure^[49-54] in one-component liquids associated with DH^[46-48]. However, DH in pure liquids generally results in a distribution of barriers or relaxation times^[71, 72], which is likely present to some degree for the problem of penetrant diffusion in glass-forming polymer networks. The pristine DH physics in pure supercooled liquids is typically manifested in a decoupling relation of the form $D_p \tau_{\alpha,p} \propto \tau_{\alpha,p}^\delta$, where the exponent δ is modestly greater than zero. Hence, there may be two competing effects of different physical origins that can induce decoupling of penetrant diffusivity and relaxation, and which go in opposite directions with increased supercooling. As shown in our companion simulation paper ^[58], if the penetrant alpha time extracted from the intermediate scattering function (ISF) adopts the 1/e decay criterion to define a relaxation time, then the DH effects are relatively weak as indicated by the product $D_p \tau_{\alpha,p}$ decreasing with T_g/T due to the mesh confinement effect per Eq(2). However, if the penetrant alpha time is extracted using a longer timescale criterion (the ISF decays to 0.1), then larger DH effects are present resulting in our finding that the product $D_p \tau_{\alpha,p}$ increases with T_g/T corresponding to the entropic mesh confinement effect becoming of second order importance.

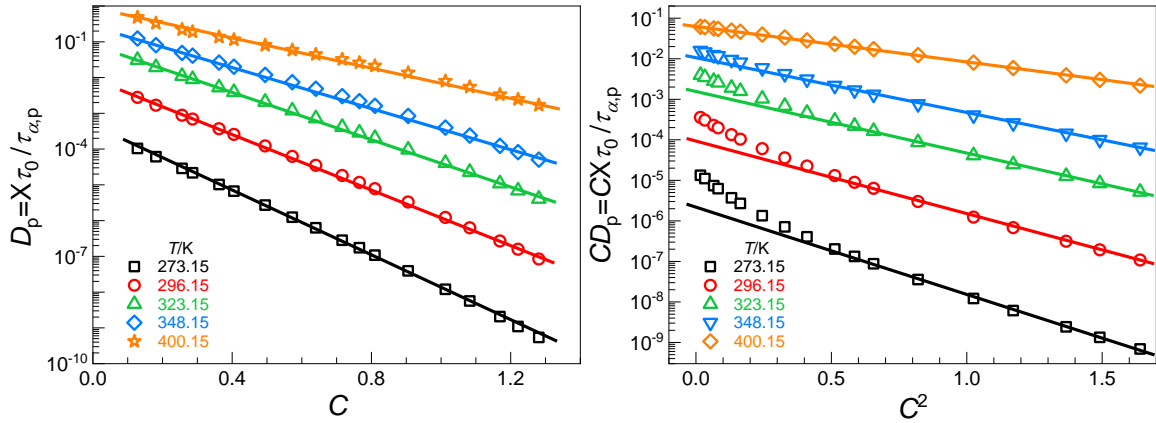


Fig.13. (a) Penetrant diffusion constant D_p as a function of confinement parameter C at various temperatures with $C = 1.94(d/\sigma)(f_n/0.19)^{1/2}$. (b) Same display as (a) but for the square power law relationship between CD_p and C .

Finally, we consider our diffusion constant predictions as a function of the mesh confinement variable. Combining the exponential relation between $\log(\tau_{\alpha,p})$ and C or C^2 predicted by SCCH theory, with an additional mesh confinement contribution per $X = \exp(-b'C)$ or $\exp(-C^2)/C$, one deduces from Eqs.(3) or (2) a net exponential relationship of the form $1/D_p \sim \exp(-EC)$ or $1/CD_p \sim \exp(-BC^2)$, respectively. Figures 13a and 13b plots the theoretical penetrant diffusion constants as a function of C and C^2 , respectively, over a wide range of temperatures and crosslink densities. One finds the diffusion constant data behaves nearly the same as that of inverse alpha time observed in Fig.10 in the following sense: (i) the diffusion constant varies exponentially with C or C^2 , and the corresponding linearity is even better (slightly worse for the C^2 relation since the local cage barrier dominates the dynamics of penetrant while its elastic barrier is negligible) than that of inverse penetrant alpha time shown in Fig.10; (ii) the effective slope (Table 1) of the logarithm of inverse diffusion constant versus C or C^2 decreases with temperature; and (iii) the diffusion constants increase with temperature. SCCH theory predicts that the elastic barrier will increase significantly as the degree of effective supercooling grows sufficiently large (increasing penetrant size or crosslink density and/or decreasing temperature), and then both the local cage and elastic barriers are crucial for penetrant hopping. In this situation, the net consequence of these two barriers results in a predicted square law relation between the *total* barrier and C , and hence one expects in practice a $\log(CD_p) \sim C^2$ law will eventually emerge in the high degree of supercooling regime.

We have verified that all our conclusions above deduced from numerical computations for the diffusion constant remain qualitatively robust regardless of the T_g criterion and choice of the prefactor A (1.94 is adopted in Figs.12 and 13) in defining confinement parameter C .

VII. Summary and Conclusions

We have carried out a detailed theoretical study of how permanent crosslinking in polymer networks impacts the relaxation and diffusivity of dilute spherical penetrants over a wide range of temperatures, crosslink densities, and T_g criteria. The key new methodological aspect is a general extension of the SCCH theory of penetrant relaxation to address the dynamic consequences of chemical crosslinking based on a segment pinning model where the local structure remains unchanged but the microscopic dynamic constraints encountered by a penetrant from its Kuhn segment neighbors is significantly intensified as crosslink density increases. This results in a rich behavior of penetrant relaxation and diffusivity as a function of temperature, crosslink density, and penetrant size.

The penetrant local cage barrier is predicted to dominate its alpha process while the elastic barrier remains relatively small. The local cage barrier varies linearly with the network glass transition temperature T_g , leading to an exponential increase (apparent “Arrhenius”) of the isothermal penetrant alpha relaxation time with $T_g(f_n)/T$. Numerical calculations based on the ECNLE theory of polymer networks reveals a proportionality between T_g and the square root of the crosslink fraction. We note that both T_g and f_n are properties of the pure polymer matrix, and hence the activated dynamics of a penetrant of fixed size is dominated by its coupling with the polymer network alpha process.

Glassy segmental scale dynamics and mesh confinement glass physics are in general both important for penetrant diffusivity, and their effects on the crosslink fraction dependence of the activation barrier are predicted to obey a remarkable degeneracy (linear in C or linear in $T_g(f_n)/T$) due to the relation $C = d/a_x = A(d/\sigma)f_n^{1/2}$. However, at fixed crosslink density, the penetrant diffusivity is a strong function of temperature, a hallmark of the importance of glassy segmental

dynamics absents in the entropy-based mesh confinement effect. Overall, the latter plays an increasing minor role compared to the consequence of crosslinking induced slowing down of polymer segmental relaxation as the degree of polymer network supercooling is increased and/or (we expect) when penetrants become sufficiently small compared to the mesh size. However, mesh confinement does slow down mass transport to varying degrees, but seemingly not the more spatially local penetrant alpha relaxation process. This results in diffusion being more strongly suppressed with increasing crosslink density than penetrant alpha relaxation, a novel form of “decoupling” of an opposite nature than the generic Stokes-Einstein breakdown^[49-54] phenomenon in glass-forming liquids.

The mechanistic coupling between activated dynamics of the penetrant and network Kuhn segments at the correlated displacement level has been elucidated, and further quantified by the decoupling time ratio defined as the ratio of the penetrant to Kuhn segment alpha relaxation times. This decoupling ratio varies non-monotonically as the degree of effective supercooling degree grows (increasing $T_g(f_n)/T$ via lowering temperature or increasing crosslink density), and sharply decreases in the deeply supercooled regime. The latter behavior arises because of the relative unimportance of the elastic barrier for penetrant hopping versus its high importance for Kuhn segment relaxation in fragile polymer networks. A remarkably good (but not perfect) collapse of the decoupling ratio as a function of $T_g(f_n)/T$ for all crosslink densities and temperatures studied is predicted, independent of the vitrification timescale adopted to define the glass transition temperature and the precise value of the polymer network strand persistence length.

Overall, we believe that the generic theoretical insights and specific predictions obtained will be useful for designing new polymer networks to optimize the absolute and relative (e.g., for selectivity applications) penetrant diffusion rates relevant to polymer-based membrane

separations. Extensions of the theory to other penetrant sizes, inclusion of penetrant-polymer attractions, under pressure, and in the glassy state (thermosets) and vitrimers^[73-76] is possible and will be studied in future work.

Acknowledgement

This research was supported by the U.S. Department of Energy, Office of Basic Energy Sciences, Division of Materials Sciences and Engineering (Award No. DE-SC0020858), through the Materials Research Laboratory at the University of Illinois at Urbana-Champaign. Helpful discussions with Christopher Evans are gratefully acknowledged.

Appendix: Effect of Persistence Length Choice

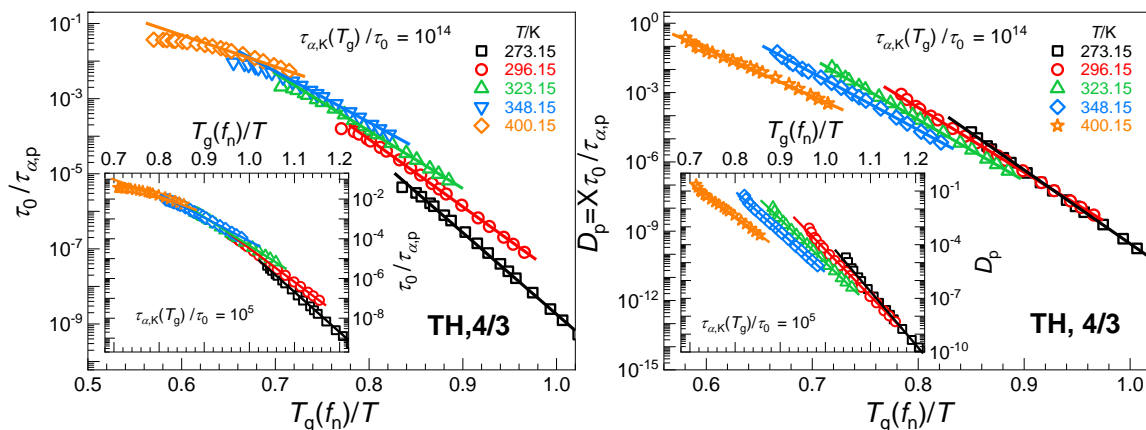


Fig.S1. Penetrant (a) inverse mean alpha time and (b) diffusion constant as a function of $T_g(f_n)/T$ at various temperatures using a $\tau_{\alpha,K}(T_g)/\tau_0 = 10^{14}$ criterion. Same displays as that of the main text Fig.8 and Fig.12, respectively, but using the $l_p/\sigma = 4/3$ local aspect ratio model. Both insets are the corresponding results for a simulation-like $\tau_{\alpha,K}(T_g)/\tau_0 = 10^5$ vitrification criterion.

References

1. D. Peer, J. M. Karp, S. Hong, O. C. Farokhzad, R. Margalit, and R. Langer, Nat. Nanotechnol. **2**, 751-760 (2007).
2. J. Guan, B. Wang, and S. Granick, ACS Nano **8**, 3331-3336 (2014).

3. K. Paeng, H. Park, D. T. Hoang, and L. J. Kaufman, *Proc. Natl. Acad. Sci. USA* **112**, 4952-4957 (2015).
4. Y. Lu, A. A. Aimetti, R. Langer, and Z. Gu, *Nat. Rev. Mater.* **2**, 1-17 (2016).
5. T. Sentjabrskaja, E. Zaccarelli, C. De Michele, F. Sciortino, P. Tartaglia, T. Voigtmann, S. U. Egelhaaf, and M. Laurati, *Nat. Commun.* **7**, 11133 (2016).
6. R. Poling-Skutvik, R. C. Roberts, A. H. Slim, S. Narayanan, R. Krishnamoorti, J. C. Palmer, and J. C. Conrad, *J. Phys. Chem. Lett.* **10**, 1784-1789 (2019).
7. M. Kanduč, W. K. Kim, R. Roa, and J. Dzubiella, *ACS nano* **15**, 614-624 (2020).
8. C. Xue, X. Shi, Y. Tian, X. Zheng, and G. Hu, *Nano Lett.* **20**, 3895-3904 (2020).
9. G. S. Sheridan and C. M. Evans, *Macromolecules* **54**, 11198-11208 (2021).
10. D. F. Sanders, Z. P. Smith, R. Guo, L. M. Robeson, J. E. McGrath, D. R. Paul, and B. D. Freeman, *Polymer* **54**, 4729-4761 (2013).
11. J. Li and D. J. Mooney, *Nat. Rev. Mater.* **1**, 1-17 (2016).
12. J. S. Vrentas and C. M. Vrentas, *Diffusion and mass transfer* (CRC Press, Boca Raton, 2016).
13. M. Galizia, W. S. Chi, Z. P. Smith, T. C. Merkel, R. W. Baker, and B. D. Freeman, *Macromolecules* **50**, 7809-7843 (2017).
14. C. R. Bilchak, M. Jhalaria, Y. Huang, Z. Abbas, J. Midya, F. M. Benedetti, D. Parisi, W. Egger, M. Dickmann, and M. Minelli, *ACS nano* **14**, 17174-17183 (2020).
15. P. Bernardo, E. Drioli, and G. Golemme, *Ind. Eng. Chem. Res.* **48**, 4638-4663 (2009).
16. G. M. Geise, H. S. Lee, D. J. Miller, B. D. Freeman, J. E. McGrath, and D. R. Paul, *J. Polym. Sci. B-Polym. Phys.* **48**, 1685-1718 (2010).
17. D. S. Sholl and R. P. Lively, *Nature* **532**, 435-437 (2016).
18. J. W. Barnett and S. K. Kumar, *Soft matter* **15**, 424-432 (2019).
19. S. R. White, N. R. Sottos, P. H. Geubelle, J. S. Moore, M. R. Kessler, S. Sriram, E. N. Brown, and S. Viswanathan, *Nature* **409**, 794-797 (2001).
20. B. J. Blaiszik, S. L. B. Kramer, S. C. Olugebefola, J. S. Moore, N. R. Sottos, and S. R. White, *Ann. Rev. Mater. Res.* **40**, 179-211 (2010).
21. J. F. Patrick, M. J. Robb, N. R. Sottos, J. S. Moore, and S. R. White, *Nature* **540**, 363-370 (2016).
22. B. D. Paulsen, K. Tybrandt, E. Stavrinidou, and J. J. N. m. Rivnay, **19**, 13-26 (2020).
23. H. Wang, J. K. Keum, A. Hiltner, E. Baer, B. Freeman, A. Rozanski, and A. Galeski, *Science* **323**, 757-760 (2009).
24. C. Wang, Q. Ge, D. Ting, D. Nguyen, H.-R. Shen, J. Chen, H. N. Eisen, J. Heller, R. Langer, and D. Putnam, *Nature Mater.* **3**, 190-196 (2004).

25. D. Li, X. Zhang, J. Yao, G. P. Simon, and H. Wang, *Chem. Commun.* **47**, 1710-1712 (2011).
26. W. Ali, B. Gebert, T. Hennecke, K. Graf, M. Ulbricht, and J. S. Gutmann, *Acs Appl. Mater. Interfaces* **7**, 15696-15706 (2015).
27. G. M. Geise, D. R. Paul, and B. D. Freeman, *Prog. Polym. Sci.* **39**, 1-42 (2014).
28. J. S. Vrentas and J. L. Duda, *J. Polym. Sci. B-Polym. Phys.* **15**, 403-416 (1977).
29. W. J. Koros and R. Mahajan, *J. Membr. Sci.* **175**, 181-196 (2000).
30. N. Ramesh, P. K. Davis, J. M. Zielinski, R. P. Danner, and J. L. Duda, *J. Polym. Sci. B-Polym. Phys.* **49**, 1629-1644 (2011).
31. K. Zhang and S. K. Kumar, *ACS Macro Lett.* **6**, 864-868 (2017).
32. D. Meng, K. Zhang, and S. K. Kumar, *Soft matter* **14**, 4226-4230 (2018).
33. K. Zhang, D. Meng, F. Müller-Plathe, and S. K. Kumar, *Soft matter* **14**, 440-447 (2018).
34. B. Mei and K. S. Schweizer, *Macromolecules* **55**, 9134-9151 (2022).
35. B. Mei, Y. Zhou, and K. S. Schweizer, *J. Phys. Chem. B* **124**, 6121-6131 (2020).
36. S. Mirigian and K. S. Schweizer, *J. Chem. Phys.* **140**, 194506 (2014).
37. Y. Zhou, B. Mei, and K. S. Schweizer, *J. Chem. Phys.* **156**, 114901 (2022).
38. B. Mei, Y. Zhou, and K. S. Schweizer, *Macromolecules* **54**, 10086-10099 (2021).
39. S. J. Xie and K. S. Schweizer, *Macromolecules* **49**, 9655-9664 (2016).
40. S. Mirigian and K. S. Schweizer, *Macromolecules* **48**, 1901-1913 (2015).
41. B. Mei, T.-W. Lin, G. S. Sheridan, C. M. Evans, C. E. Sing, and K. S. Schweizer, *Macromolecules* **55**, 4159-4173 (2022).
42. B. Mei and K. S. Schweizer, *Soft Matter* **17**, 2624-2639 (2021).
43. R. Zhang and K. S. Schweizer, *J. Chem. Phys.* **146**, 194906 (2017).
44. B. Mei, G. S. Sheridan, C. M. Evans, and K. S. Schweizer, *Proc. Natl. Acad. Sci. USA* **119**, e2210094119 (2022).
45. B. Mei and K. S. Schweizer, *J. Chem. Phys.* **155**, 054505 (2021).
46. S. Karmakar, C. Dasgupta, and S. Sastry, *Annu. Rev. Condens. Matter Phys.* **5**, 255-284 (2014).
47. L. Berthier and G. Biroli, *Rev. Mod. Phys.* **83**, 587-645 (2011).
48. B. Mei, B. Zhuang, Y. Lu, L. An, and Z.-G. Wang, *J. Phys. Chem. Lett.* **13**, 3957-3964 (2022).
49. C. K. Mishra and R. Ganapathy, *Phys. Rev. Lett.* **114**, 198302 (2015).
50. H. B. Yu, K. Samwer, Y. Wu, and W. H. Wang, *Phys. Rev. Lett.* **109**, 095508 (2012).

51. L. Xu, F. Mallamace, Z. Yan, F. W. Starr, S. V. Buldyrev, and H. E. Stanley, *Nature Phys.* **5**, 565-569 (2009).
52. S. K. Kumar, G. Szamel, and J. F. Douglas, *J. Chem. Phys.* **124**, 214501 (2006).
53. D. N. Perera and P. Harrowell, *Phys. Rev. Lett.* **81**, 120 (1998).
54. B. Mei, Y. Lu, L. An, and Z.-G. Wang, *Phys. Rev. E* **100**, 052607 (2019).
55. L.-H. Cai, S. Panyukov, and M. Rubinstein, *Macromolecules* **48**, 847-862 (2015).
56. Z. Xu, X. Dai, X. Bu, Y. Yang, X. Zhang, X. Man, X. Zhang, M. Doi, and L.-T. Yan, *ACS nano* **15**, 4608-4616 (2021).
57. V. Sorichetti, V. Hugouvieux, and W. Kob, *Macromolecules* **54**, 8575-8589 (2021).
58. T.-W. Lin, B. Mei, K. S. Schweizer, and C. E. Sing, Submitted to *J. Chem. Phys.* (2023).
59. D. Ben-Amotz and J. Drake, *J. Chem. Phys.* **89**, 1019-1029 (1988).
60. K. S. Schweizer and E. J. Saltzman, *J. Chem. Phys.* **119**, 1181-1196 (2003).
61. A. Ghosh and K. S. Schweizer, *Macromolecules* **53**, 4366-4380 (2020).
62. K. G. Honnell, J. G. Curro, and K. S. Schweizer, *Macromolecules* **23**, 3496-3505 (1990).
63. R. Koyama, *J. Phys. Soc. Jpn.* **34**, 1029-1038 (1973).
64. X. Zheng, Y. Guo, J. F. Douglas, and W. Xia, *J. Chem. Phys.* **157**, 064901 (2022).
65. D. C. Viehman and K. S. Schweizer, *J. Chem. Phys.* **128**, 084509 (2008).
66. P. Hänggi, P. Talkner, and M. Borkovec, *Rev. Mod. Phys.* **62**, 251-341 (1990).
67. H. A. Kramers, *Physica* **7**, 284-304 (1940).
68. D. Walsh and P. Zoller, *Standard pressure volume temperature data for polymers* (CRC press, 1995).
69. B. Mei, Y. Zhou, and K. S. Schweizer, *J. Phys. Chem. B* **125**, 12353-12364 (2021).
70. B. Mei, Y. Zhou, and K. S. Schweizer, *Proc. Natl. Acad. Sci. USA* **118**, e2025341118 (2021).
71. S.-J. Xie and K. S. Schweizer, *Macromolecules* **53**, 5350-5360 (2020).
72. S.-J. Xie and K. S. Schweizer, *J. Chem. Phys.* **152**, 034502 (2020).
73. L. Rovigatti, G. Nava, T. Bellini, and F. Sciortino, *Macromolecules* **51**, 1232-1241 (2018).
74. A. Perego and F. Khabaz, *Macromolecules* **53**, 8406-8416 (2020).
75. A. Perego, D. Lazarenko, M. Cloitre, and F. Khabaz, *Macromolecules* **55**, 7605-7613 (2022).
76. L. Porath, B. Soman, B. B. Jing, and C. M. Evans, *ACS Macro Lett.* **11**, 475-483 (2022).